Nuclear Structure Research at RITU

J. Uusitalo, M. Leino, J. Saren

for the JUROGAMII/SAGE + RITU + GREAT collaboration
University of Jyväskylä, Department of Physics

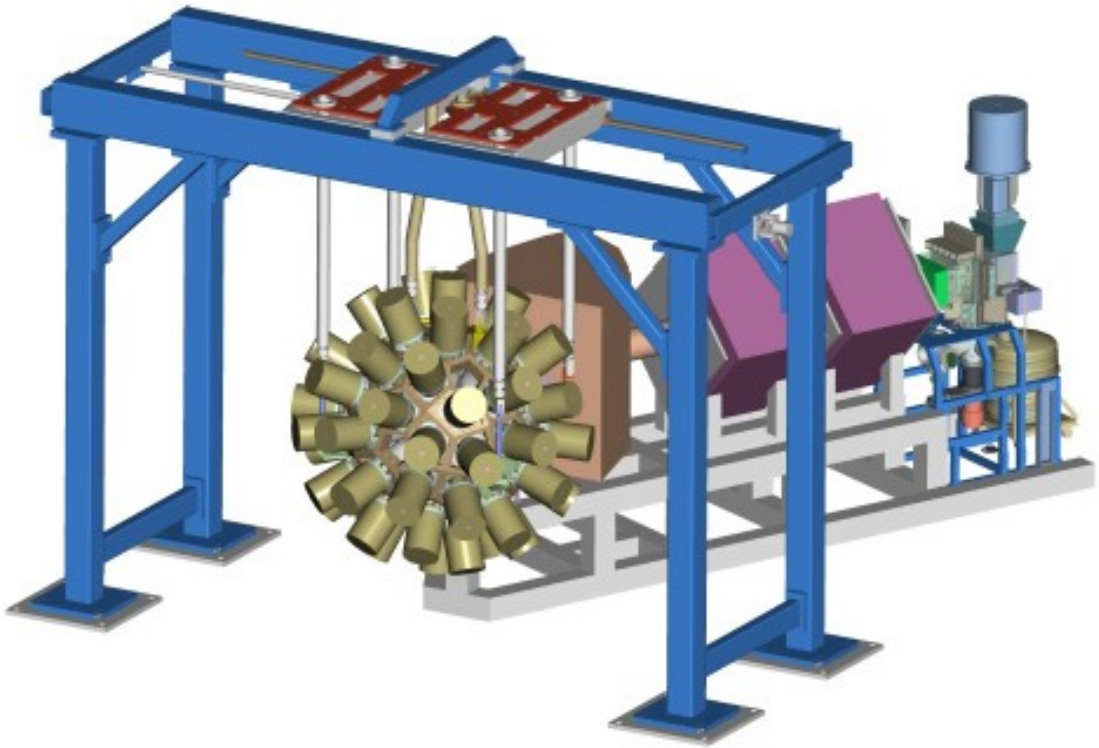

HIE-ISOLDE Spectrometer Workshop, 10-11 March 2011, Lund, Sweden

Absolute transmission of gas-filled recoil separator RITU

J. Sarén*, J. Uusitalo, M. Leino, J. Sorri

Department of Physics, University of Jyväskylä, P. O. Box 35, FI-40014, Jyväskylä, Finland

Table 1: RITU specification. See labeling of the elements in the figure 2.

Max. magnetic rigidity	2.2 Tm
Total mass	17500 kg
Horizontal/Vertical acceptance	±25/±85 mrad
Dispersion	10 mm/(1% in $B\rho$)
Dipole radius of curvature	1850 mm
Dipole maximum field	1.2 T
Dipole deflection angle	25°
Dipole gap	100 mm
Dipole entrance and exit angles	0°, -25°
Q_1 gap diameter	105 mm
Q_1 max. gradient	13.5 T/m
Q_1 optical length	350 mm
$Q_{2,3}$ gap diameter	200 mm
$Q_{2,3}$ max. gradient	6.0 T/m
$Q_{2,3}$ optical length	600 mm
Total optical length	4.8 m

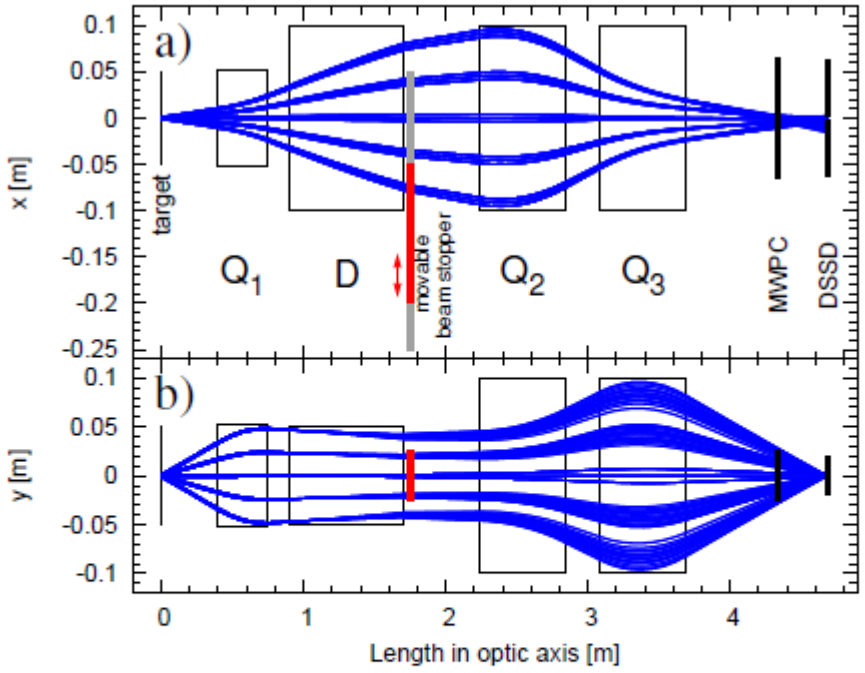

Figure 2: Ion trajectories with combinations of horizontal and vertical initial angles of 0, ±12.5, ±25 and 0, ±42.5, ±85 mrad, respectively. The mass, charge and the kinetic energy are those of a reference particle.

Magnetic separation

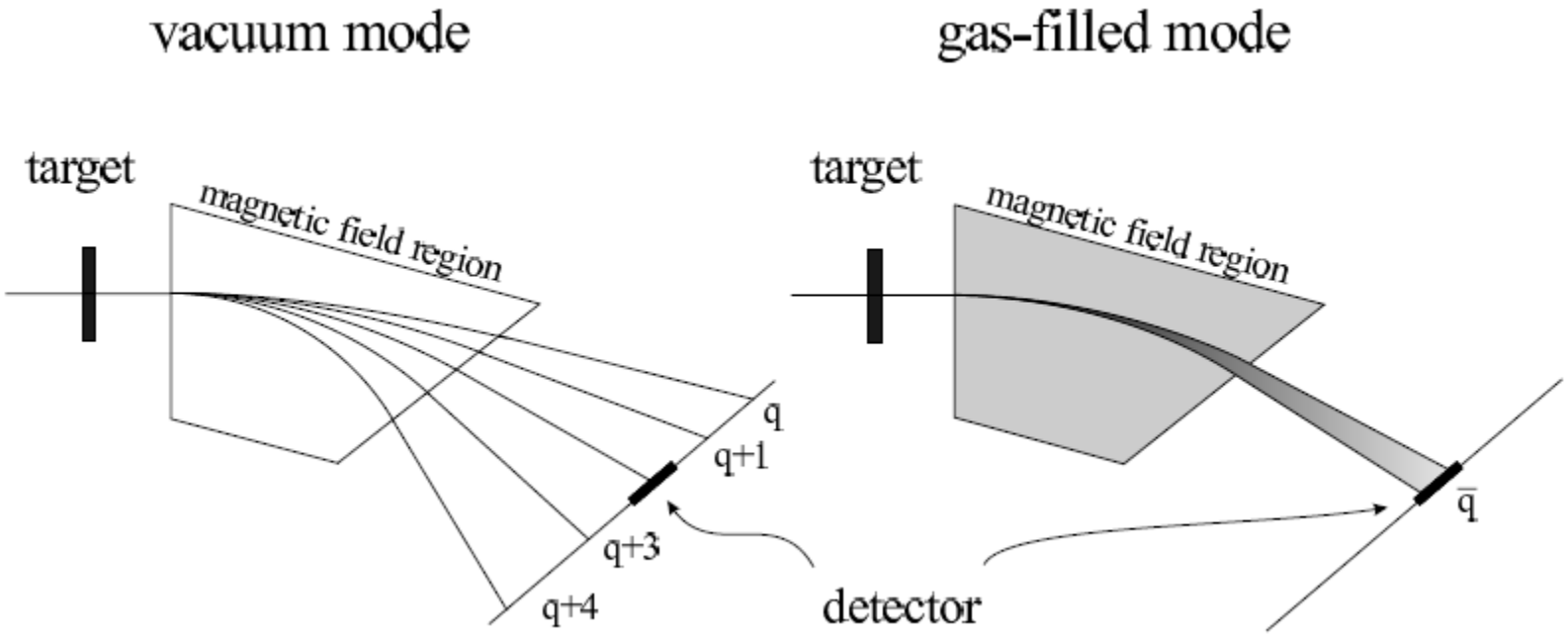

Vacuum mode

$m_b v_b/q_b \approx m_{fr} v_{fr}/q_{fr}$

Gas-filled mode

$m_b v_b/q_b < m_{fr} v_{fr}/q_{fr}$

RDT Instrumentation at JYFL in Jyväskylä, Finland

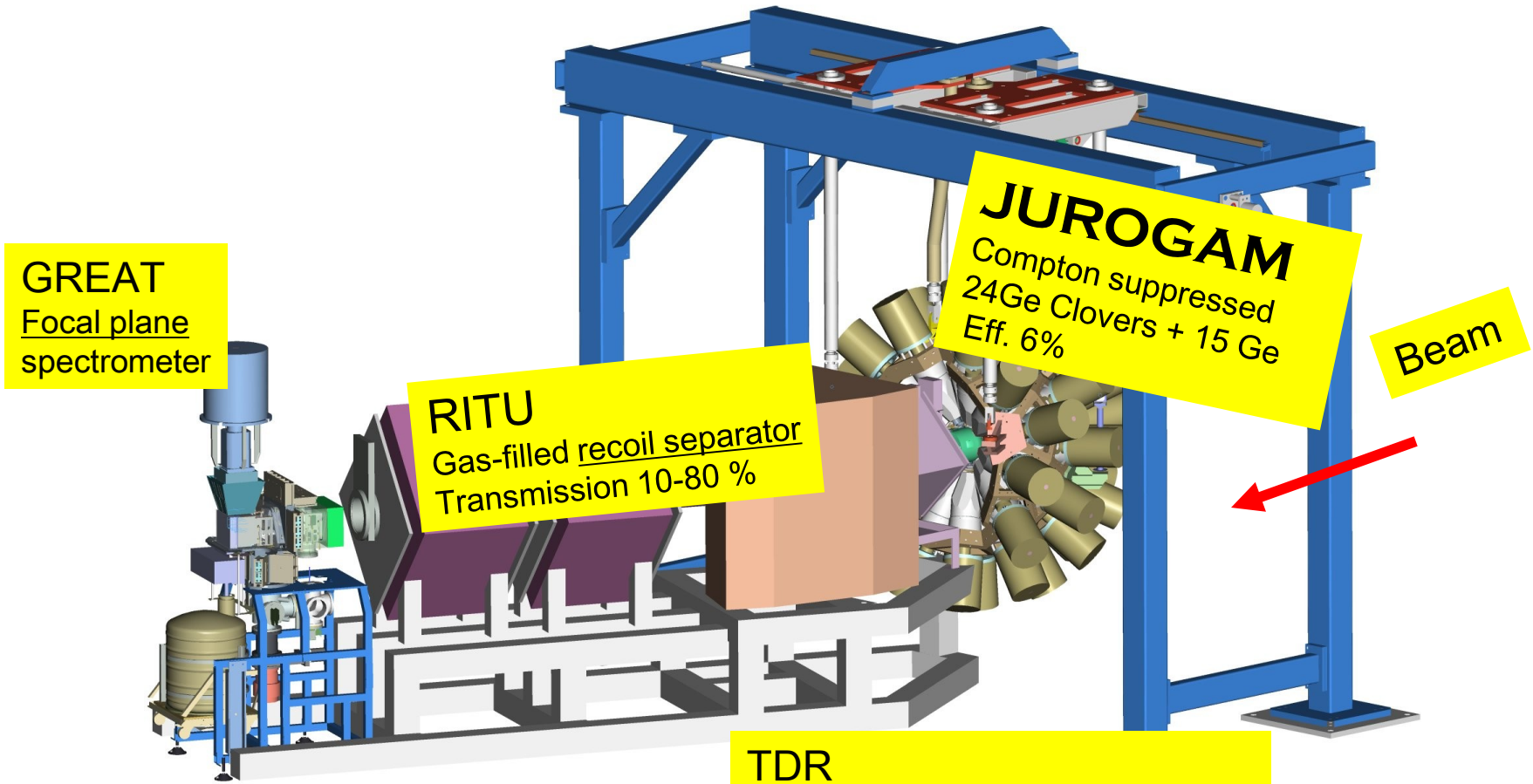

Window-less operation

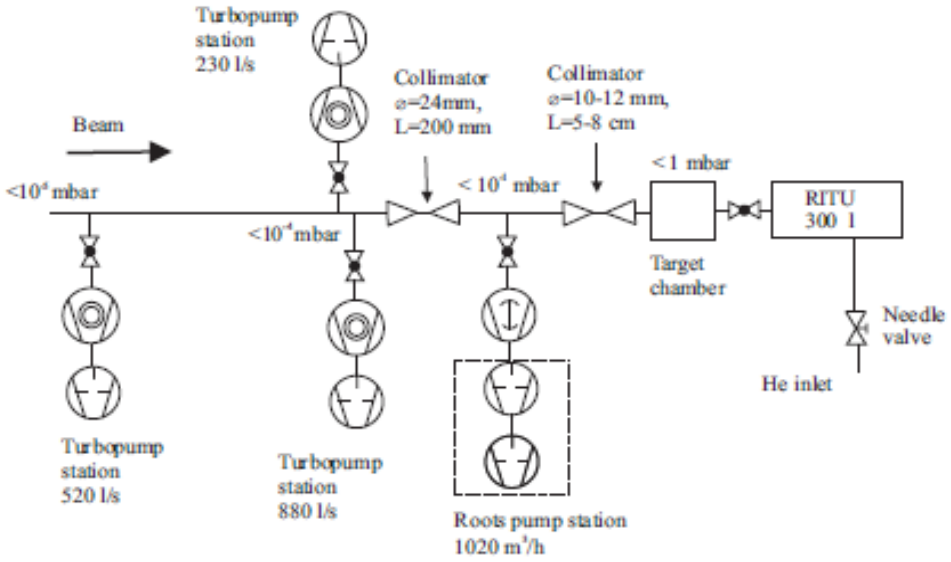

Figure 3.8: Flow chart of the differential pumping system

Window-mode operation
~ 50 µg/cm^2 Carbon foil

- in-beam electron spectroscopy
- plunger experiments
- use of high voltages and the need for a good vacuum < 10^{-6} torr

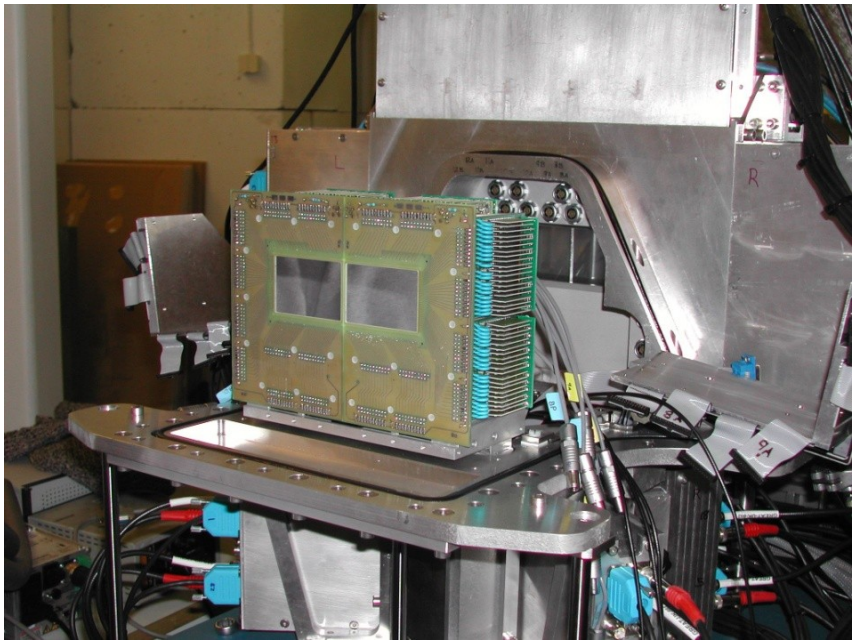


GreαT
ORTEC

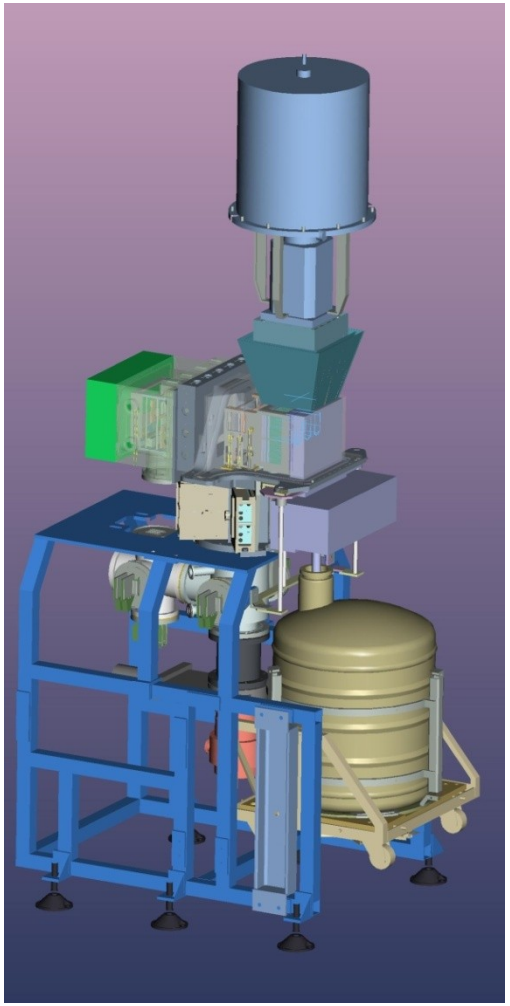

A.N. Andreyev et al. / Nuclear Instruments and Methods in Physics Research A 533 (2004) 422–434

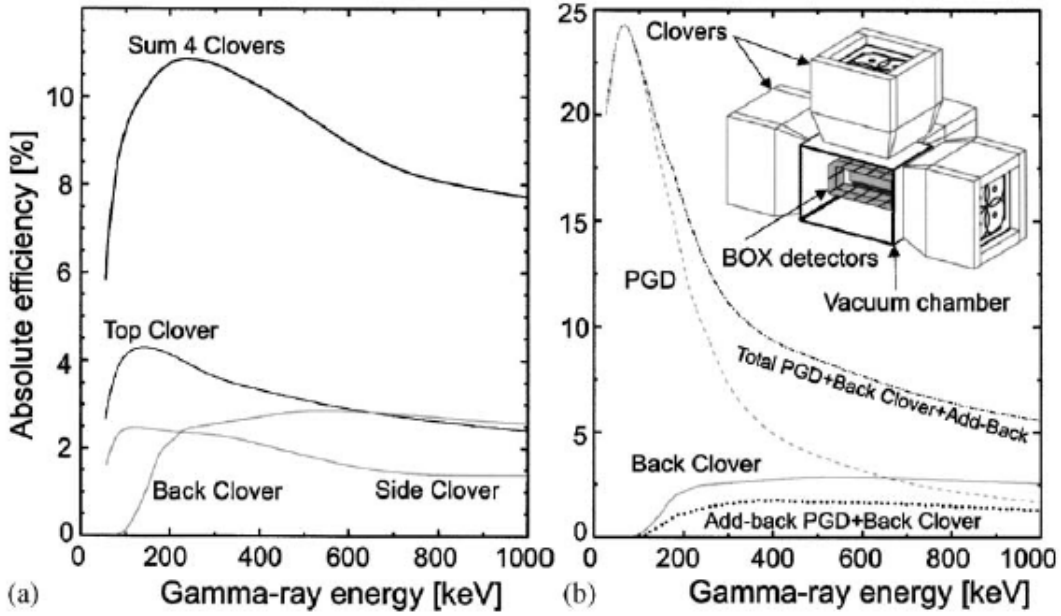

Silicon And Germanium spectrometer
SAGE

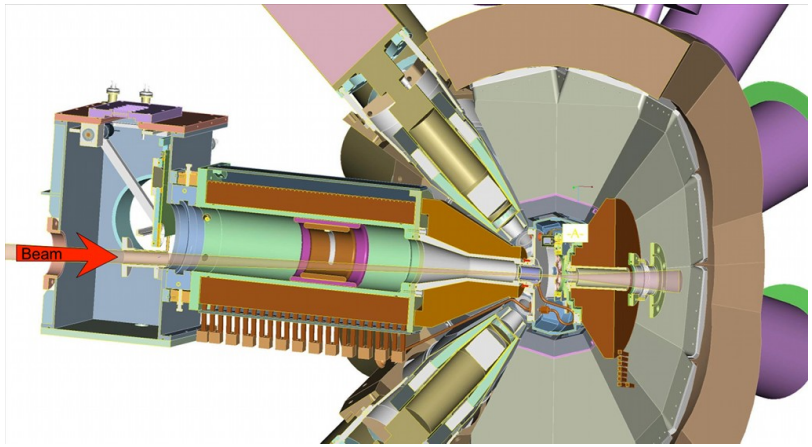

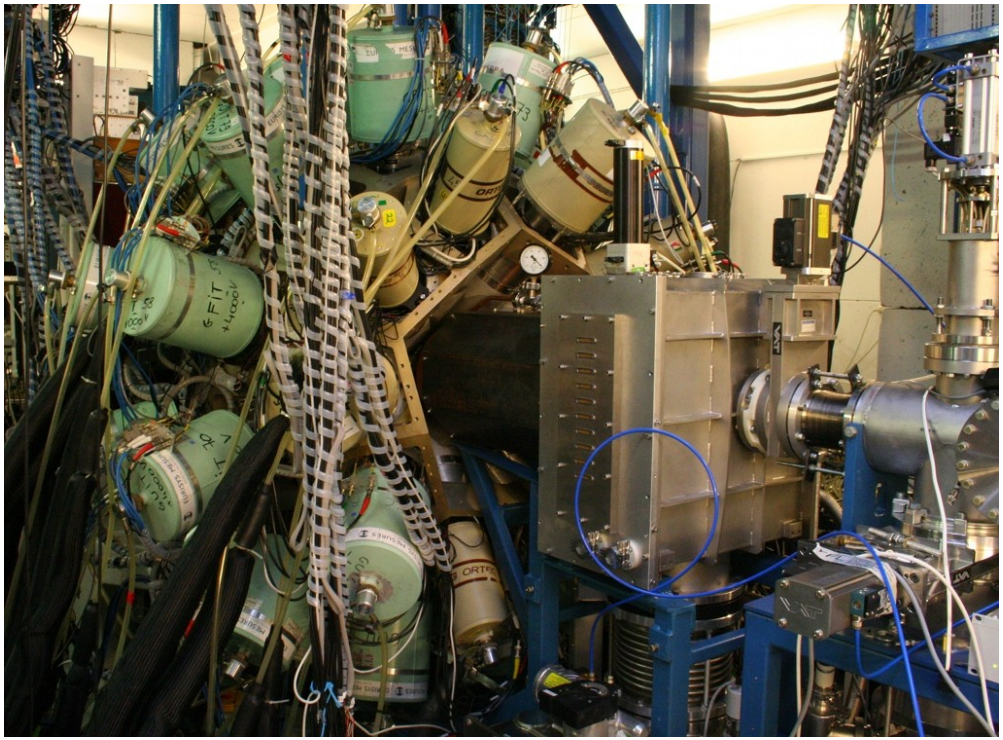

Light Ion Spectrometer Array LISA

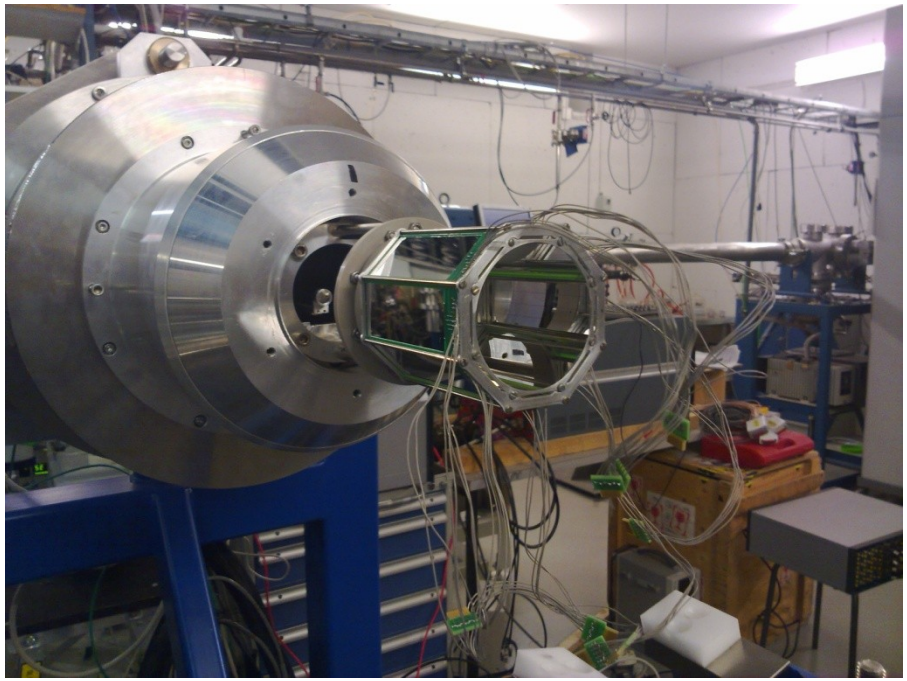

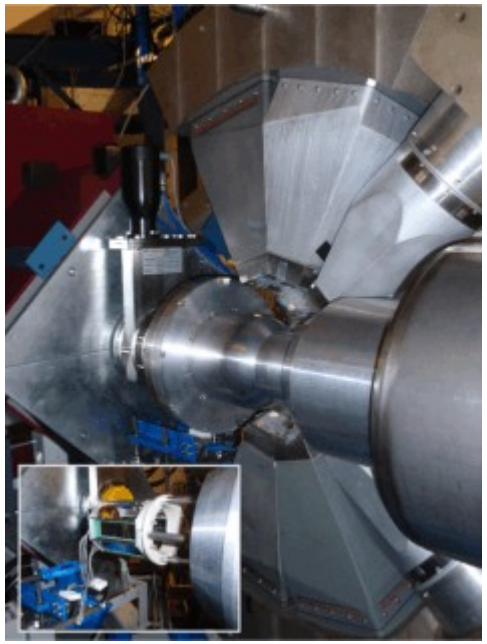

DPUNS plunger

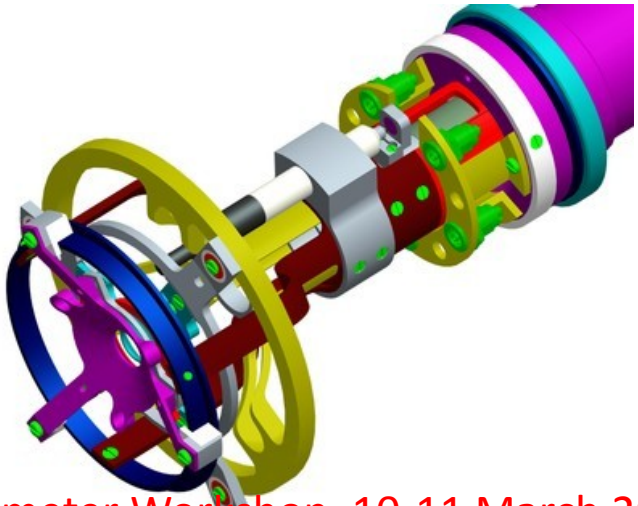

reducing the scattered beam component

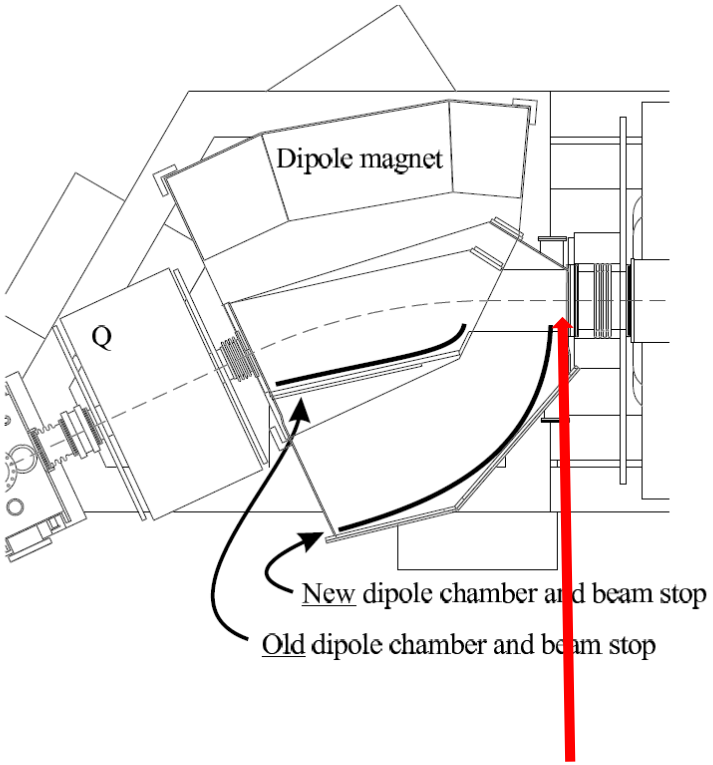

Additional beam stopper

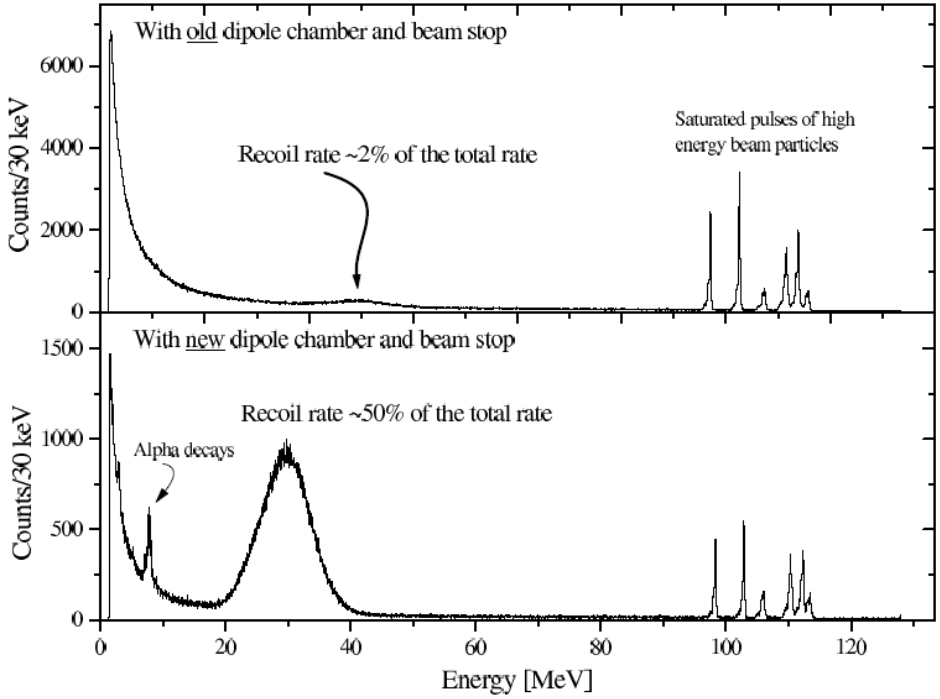

Figure 3.7: The effects of the modification of the dipole chamber and the beam stop to the energy spectra of the events observed at the focal plane silicon detector in $^{83}Kr + ^{109}Ag$ reaction. The upper spectrum is measured with the original design and the lower with the modified dipole chamber and beam stop.

Further separation

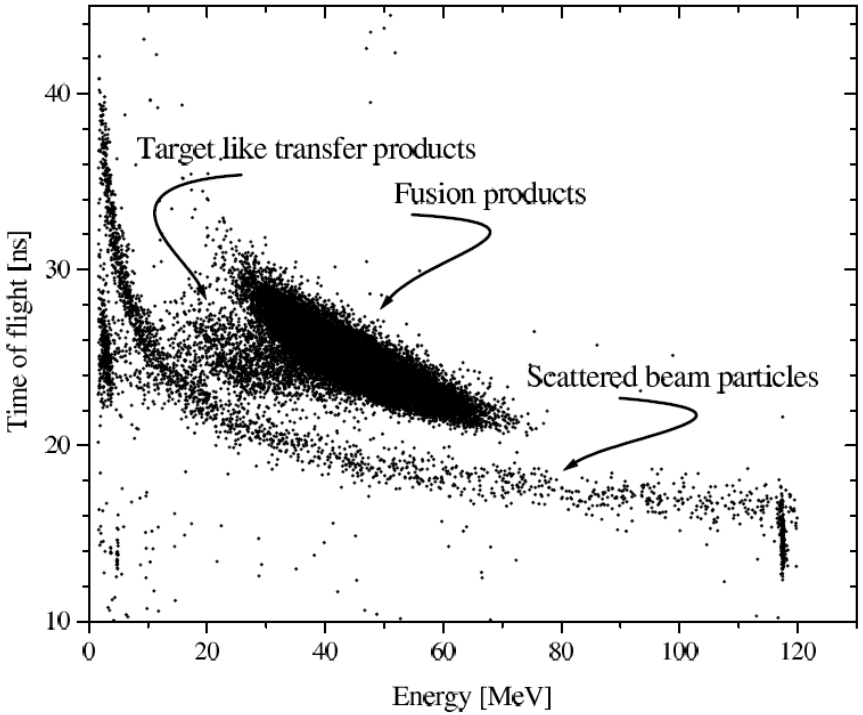

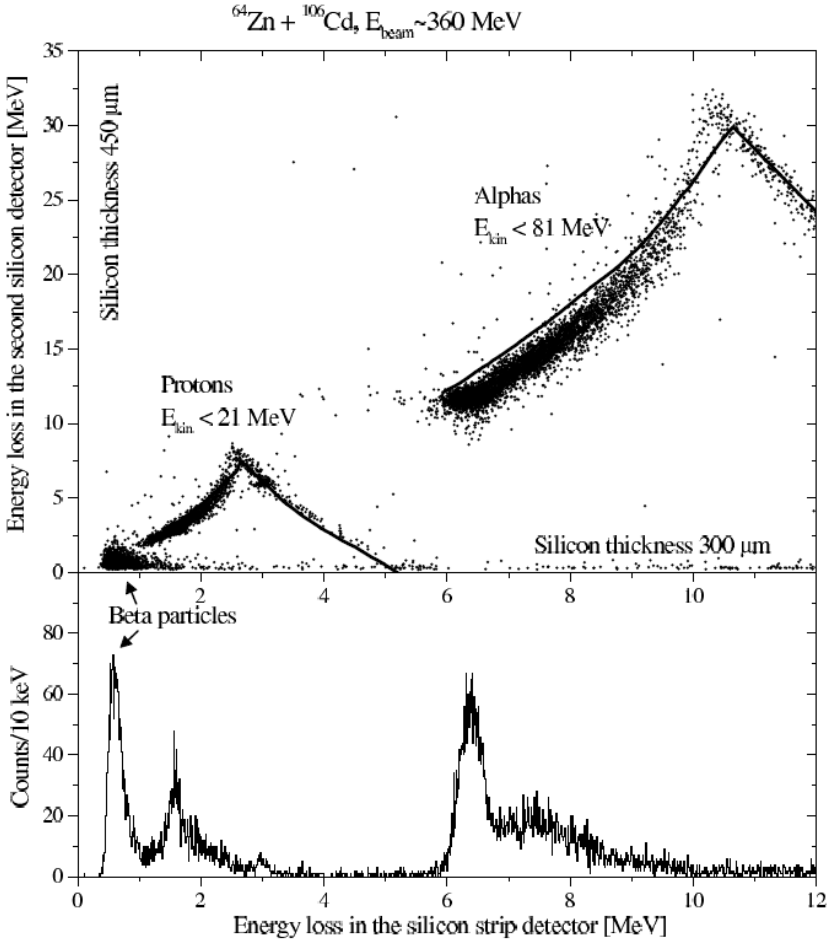

Recoil gatin RG and Recoil Decay Tagging RDT
Recoil Isomer Tagging RIT

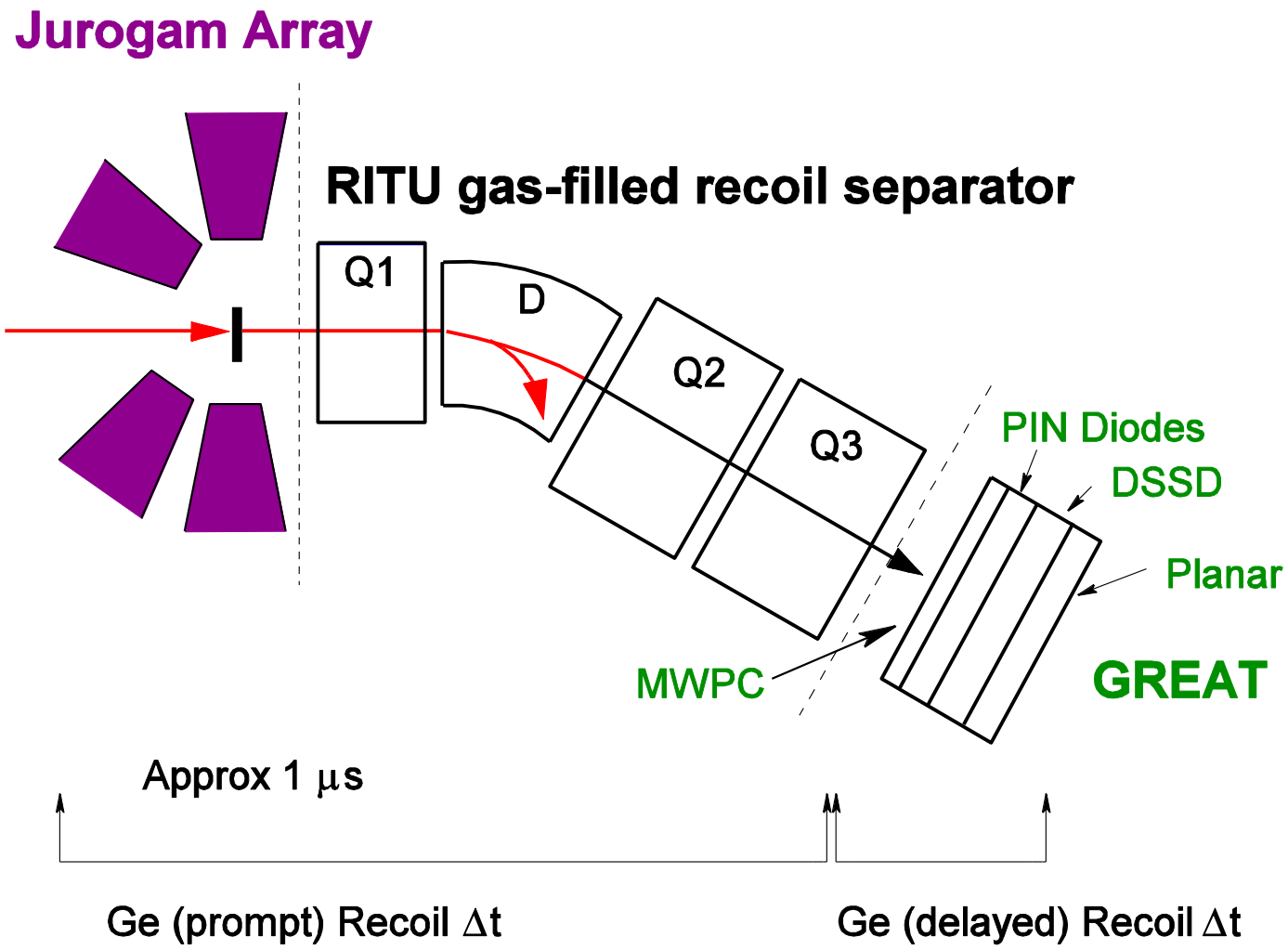

Absolute transmission measurements

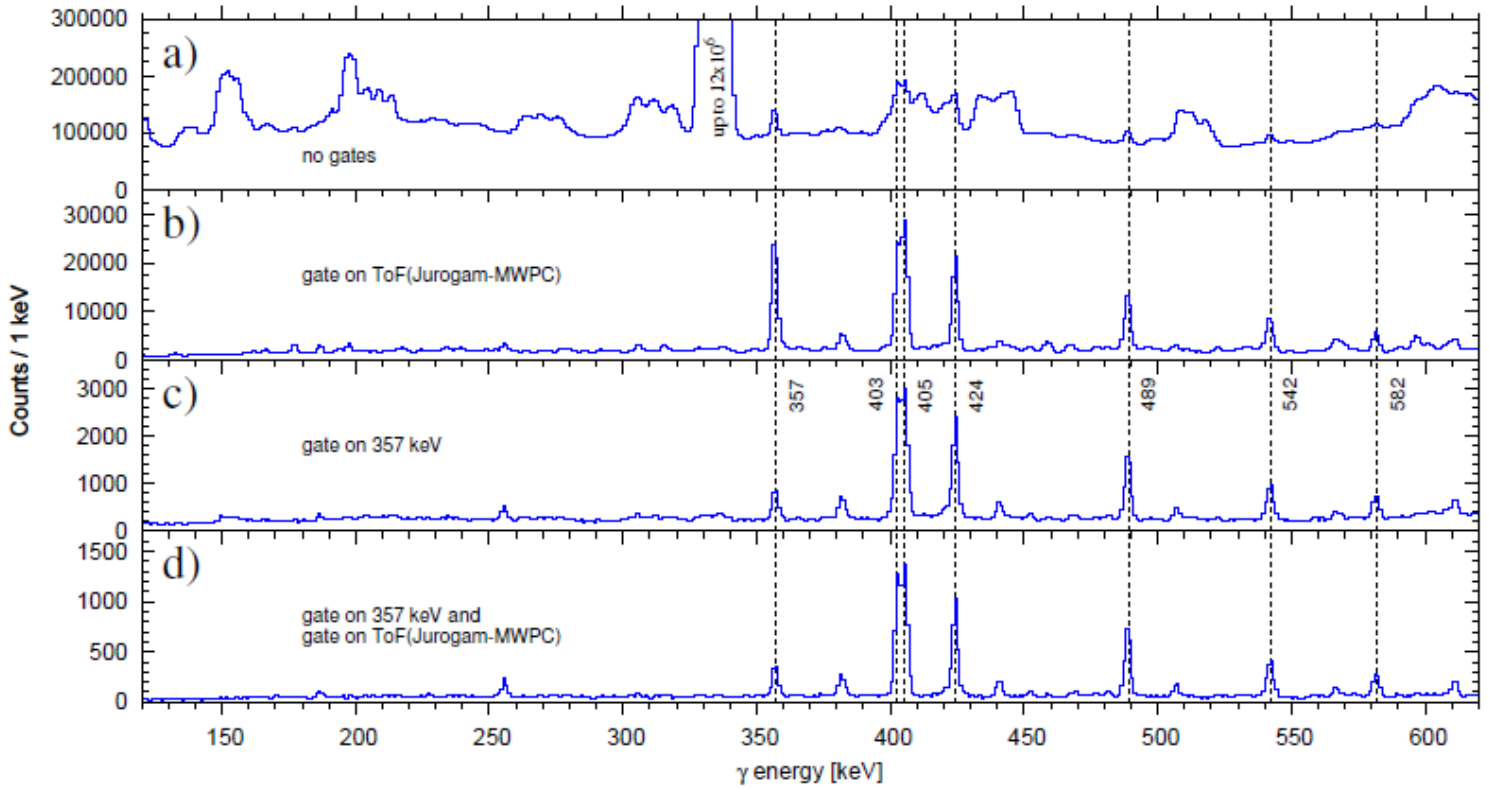

Figure 3: Prompt γ Compton suppressed spectra at the target position from the reaction ^{150}SmF(^{40}Ar,4n)^{186}Hg. Most intense transition energies of ^{186}Hg are shown with vertical lines. The panel a) shows singles γ spectrum while the panel b) shows singles spectrum of the events following the event in MWPC at a time gate. Spectra in coincidence with 357 keV γ transition (mainly $6^+ \rightarrow 4^+$) are shown with d) and without c) requiring MWPC coincidence.

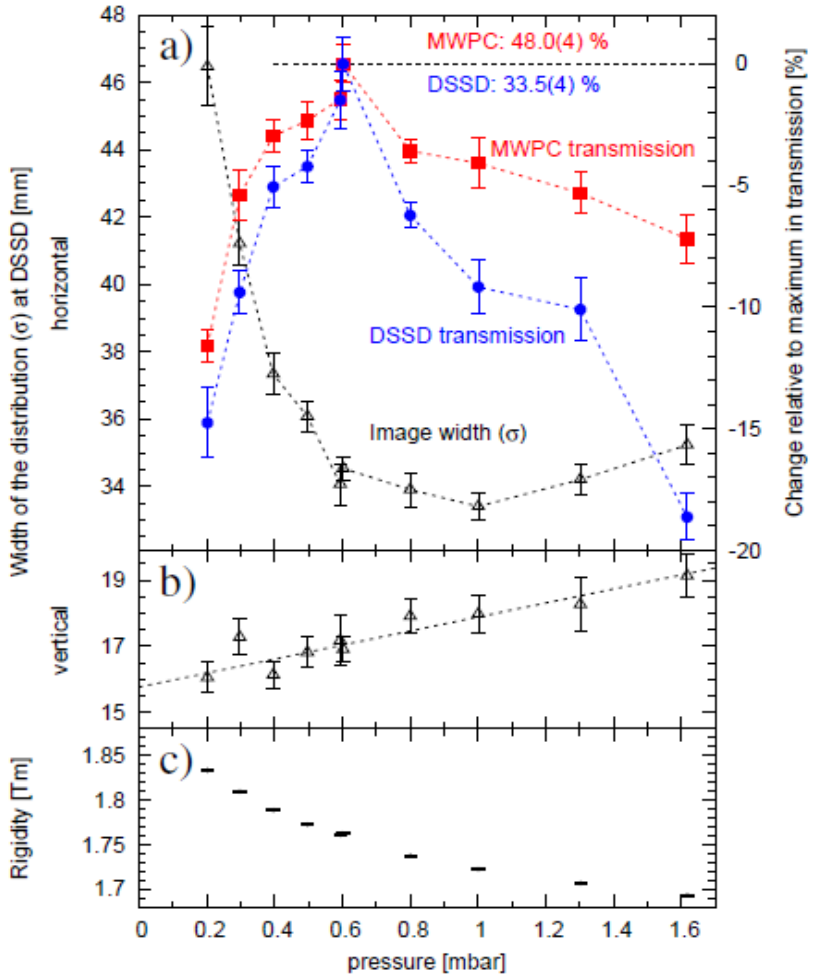

Figure 8: The position distribution widths (sigmas) in a) horizontal and b) vertical directions from the reaction ^{150}SmF(^{40}Ar,4n)^{186}Hg at different pressures. In the panel a) also the relative changes in absolute transmission are shown. The panel c) shows the magnetic rigidity behaviour in function of pressure.

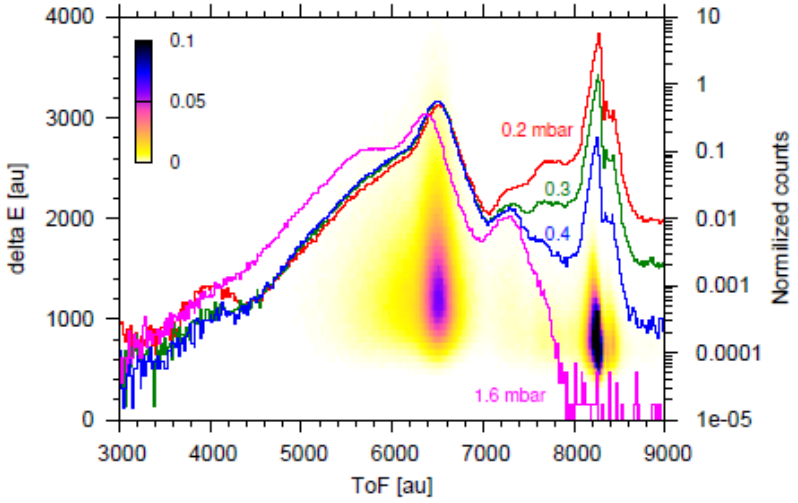

Figure 14: The energy loss in the MWPC versus time of flight (ToF) between the MWPC and the DSSD (p = 0.3 mbar) and ToF spectra with various pressures in the reaction ^{40}Ar+^{150}SmF . Particles with higher x-value are faster.

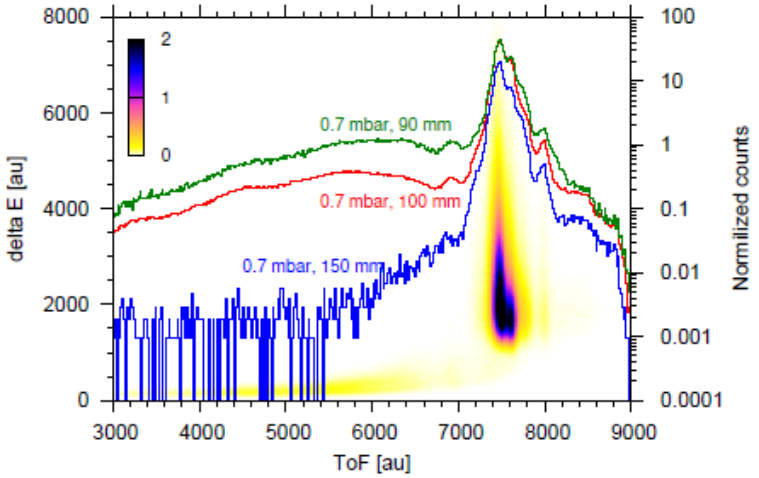

Figure 16: The energy loss in the MWPC versus time of flight between the MWPC and the DSSD (p = 0.7 mbar and the beam stopper at 100 mm) and ToF spectra with various beam stopper values in the reaction ^{84}Kr+^{nat}Mo.

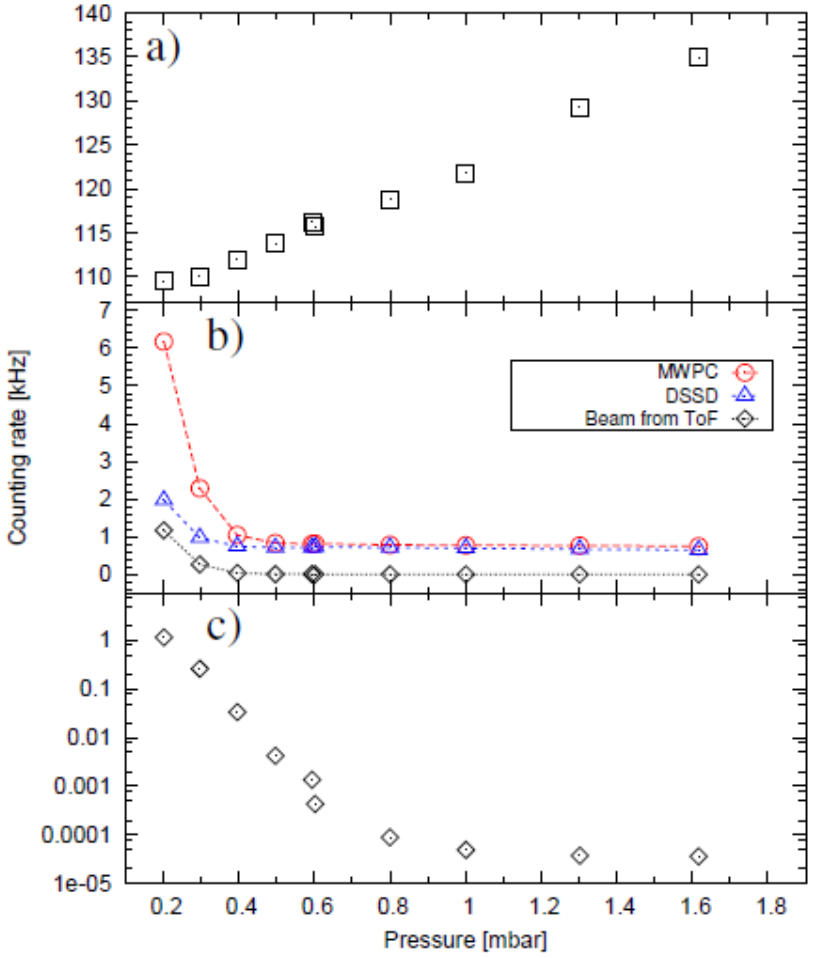

Figure 13: Counting rates of a) the Jurogam, b) the MWPC and the DSSD and c) the almost full energy beam particles in the DSSD (the datapoints of panel b) represented in a logarithmic scale) as a function of pressure in reaction ^{40}Ar+^{150}SmF. The diamonds represent the beam component integrated from ToF spectrum (MWPC-DSSD).

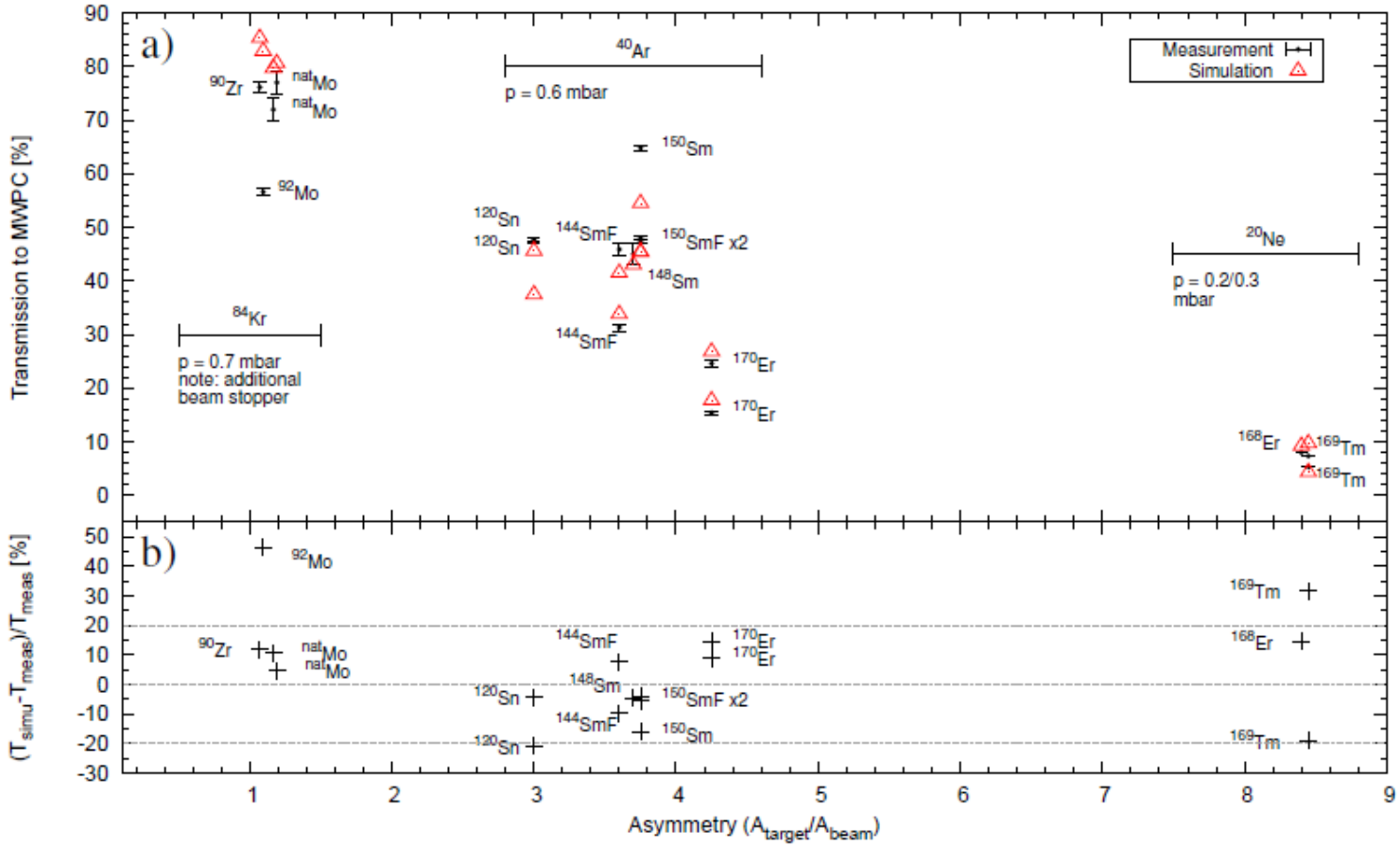

Figure 21: The observed and simulated transmissions of the studied reactions as a function of reaction asymmetry. The panel a) shows both values on an absolute scale and the panel b) the relative differences of these.

Table 2: Reactions used and measured transmissions to the MWPC and DSSD and rigidities of the products in the given gas pressure. Width of the spatial distribution at the DSSD is listed if there has been enough statistics to make a fit. In the case of ^{20}Ne beam recoils have stopped in the MWPC. The pressure and the position of the movable beam stopper used for listed properties are separately given in bold face for the reactions where gas pressure or the stopper position have been varied. The transmissions to the MWPC marked with * are corrected for off-centered distribution. The transmission values of the reaction ^{40}Ar(^{148}Sm,4n)^{184}Hg are measured with the stopper position of 60.0 mm but the values shown are corrected to represent the transmissions without the additional stopper (see figure 5).

Beam	E_{lab} [MeV]	Target	[μg/cm^2]	Pressure [mbar]	Stopper [mm]	Main channel	Transmission [%] to MWPC	Transmission [%] to DSSD	Rigidity [Tm]	Width [mm]	Height [mm]
^{40}Ar	170	^{150}SmF	250	0.2–1.6, **0.6**	0	4n + ^{186}Hg	47.7(4)	33.3(4)	1.762(2)	34.3(5)	16.9(4)
		^{144}SmF	402	0.6	0	2n + ^{182}Hg	45.9(11)	31.6(9)	1.720(2)	35.6(8)	15.3(8)
						p2n + ^{181}Au	31.3(7)	21.9(6)	1.745(2)	36.4(11)	21(3)
		^{150}Sm	200	0.6	0	4n + ^{186}Hg	64.8(6)	47.5(4)	1.760(2)	34.4(5)	15.4(4)
		^{170}Er	500	0.6	0	4n + ^{206}Rn	24.6(6)	15.7(5)	1.741(2)	35.0(7)	18.6(11)
						5n + ^{205}Rn	15.4(4)	9(3)	1.73(4)	?	?
		^{120}Sn	500	0.6	0	4n + ^{156}Er	47.7(3)	36.9(2)	1.511(2)	34.9(3)	13.65(9)
						5n + ^{155}Er	47.3(2)	36.1(2)	1.503(2)	35.0(3)	13.7(2)
^{40}Ar	188	^{148}Sm	337	0.42	5–100, **0**	4n + ^{184}Hg	45(2)	37(2)	1.755(2)	37.3(8)	11.1(4)
^{40}Ar	178	^{168}Er	500	0.39	0–140, **0**	4n + ^{204}Rn	-	-	1.730(2)	37.8(6)	16.0(4)
^{84}Kr	336	^{nat}Mo	400	0.5–1.0, **0.7**	90–150, **100**	4n + ^{180}Pt	77(2)*	66(2)	1.467(2)	41.5(8)	5.0(2)
						4n + ^{178}Pt	72(2)*	65.3(10)	1.439(2)	42.2(11)	5.2(2)
		^{90}Zr	500	0.7	90	2n + ^{172}Os	76.2(10)	71.0(11)	1.370(10)	39.6(8)	5.1(3)
		^{92}Mo	600	0.7	100	2n + ^{174}Pt	56.7(9)	49.0(10)	1.411(2)	42.4(4)	5.0(2)
^{20}Ne	95	^{168}Er	500	0.2–0.8, **0.2**	0–150, **0**	4n + ^{184}Pt	8.03(9)	-	1.674(2)	-	-
		^{169}Tm	420	0.3	0	4n + ^{185}Au	7.36(10)	-	1.609(4)	-	-
		^{169}Tm	670	0.3	0	4n + ^{185}Au	5.31(6)	-	1.604(3)	-	-

$^{208}Pb(^{48}Ca,2n)^{254}No$
- Only 2n channel, 2 µb, very strong fission competition
- Total rate ~ 1Hz/10 pnA

$^{169}Tm(^{40}Ar,6n)^{203}Fr$
- Total rate 100-300 Hz/ 10 pnA, strong fission competition

$^{96}Ru(^{78}Kr,p3n)^{170}Au$
- Total rate 2-3 kHz/ 10 pnA

$^{58}Ni(^{54}Fe,2n)^{110}Xe$
- Total rate > 1 kHz/ 1 pnA

$^{40}Ca(^{28}Si,pn)^{66}As$
- Total rate > 1 kHz/ 1pnA

10 pnA ~ 6×10^{10} p/s

$^{208}Pb(^{48}Ca,2n)^{254}No$

- Only 2n channel, 2 µb, very strong fission competition
- $\sigma_{2n} \approx \sigma_{ER} << \sigma_f$
- Total focal plane rate ~ 1Hz/10 pnA
- at the target position single detector Ge rate 5-10 kHz / 10 pnA
- with digital electronics Ge-detectors can be used at 50 kHz
- Recoil gating

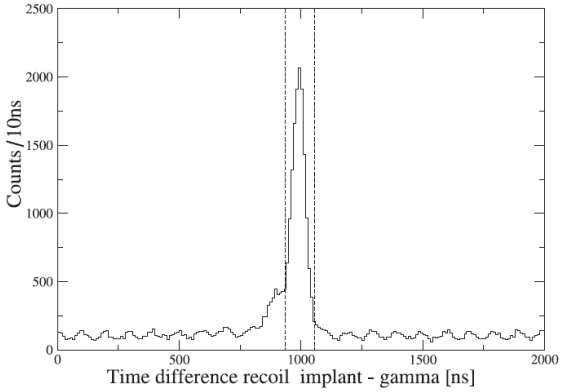

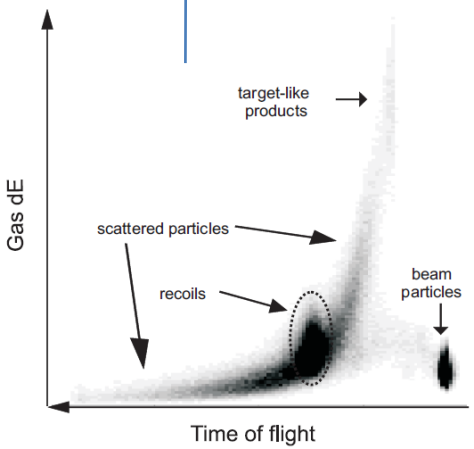

Sarah Eeckhaudt et al.,

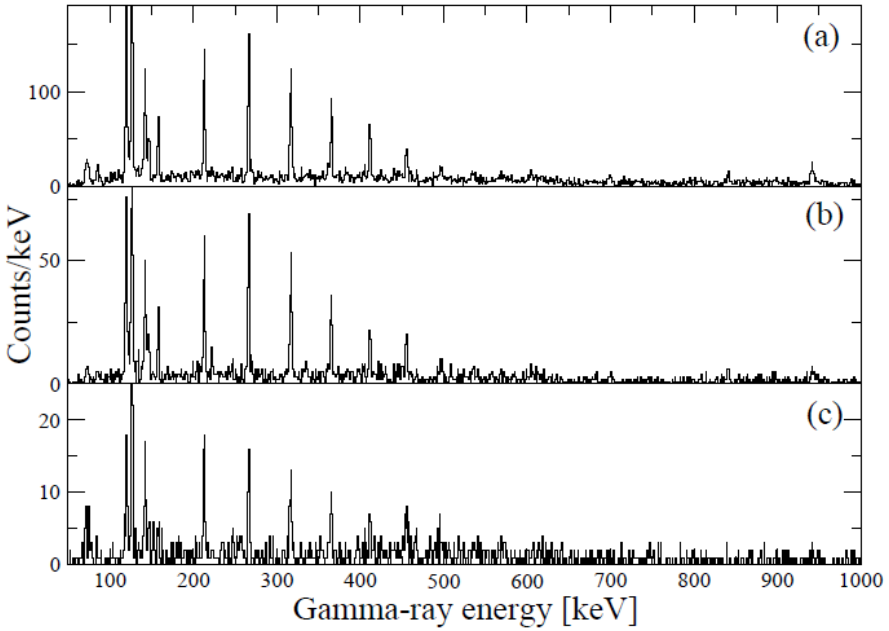

Figure 4.10: Gamma-ray singles spectra of ^{254}No with data of both beam energies combined: (a) Recoil-gated γ-ray singles spectrum (b) No-α tagged γ-ray singles spectrum (c) The recoil-gated γ-ray singles spectrum for higher beam energy only.

^{96}Ru(^{78}Kr,p3n)^{170}Au

-Total rate 2-3 kHz/ 10 pnA

- Recoil gating and α (or proton tagging)

- maximum beam intensity limited by random correlations

Heikki Kettunen et. al.,

Detector Pixel size
5 mm x 1 mm

σ_{3n} ~ 2 nb
σ_{p3n} ~ 90 nb
σ_f ~ 100 mb

Many fusion evap. channels open, no fission

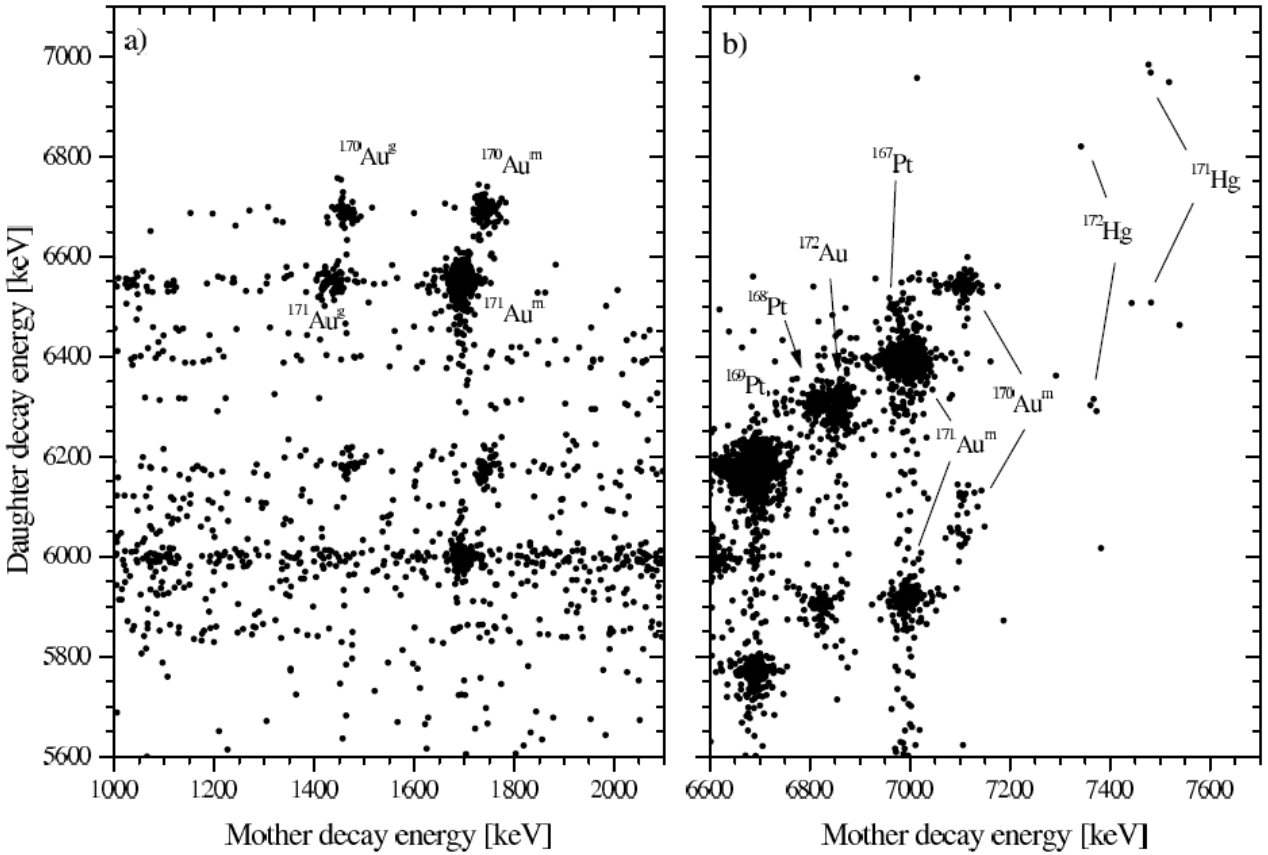

FIG. 2: Two-dimensional plot of the mother and daughter decay energies of correlated decay chains of the type ER − p_m/α_m − α_d observed in the ^{78}Kr + ^{96}Ru reaction. (a) Correlations where the proton decay of mother nucleus is followed by an α decay of the daughter nucleus (ER − p_m − α_d). (b) Correlated decay chains for α decays (ER − α_m − α_d). Maximum search times for the mother and daughter decays were 10 ms and 200 ms, respectively.

^{58}Ni(^{54}Fe,2n)^{110}Xe

-Total rate 1 kHz/ 1 pnA

- σ_{2n} ~ 20 nb << σ_f = n x 100 mb
- additional ”beam stopper” used
- Recoil gating and α-α tagging

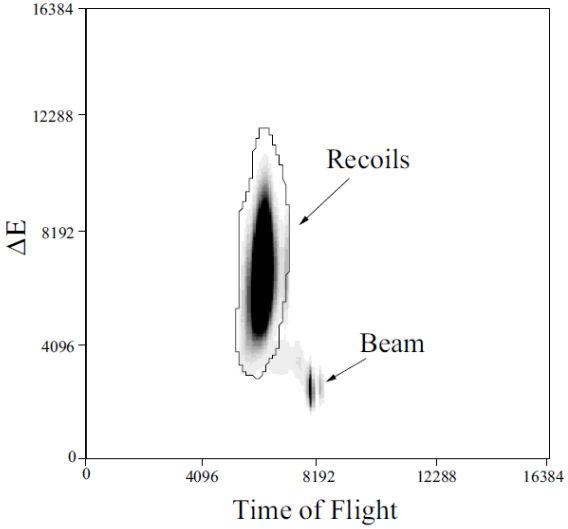

Mikael Sandzelius et. al.,

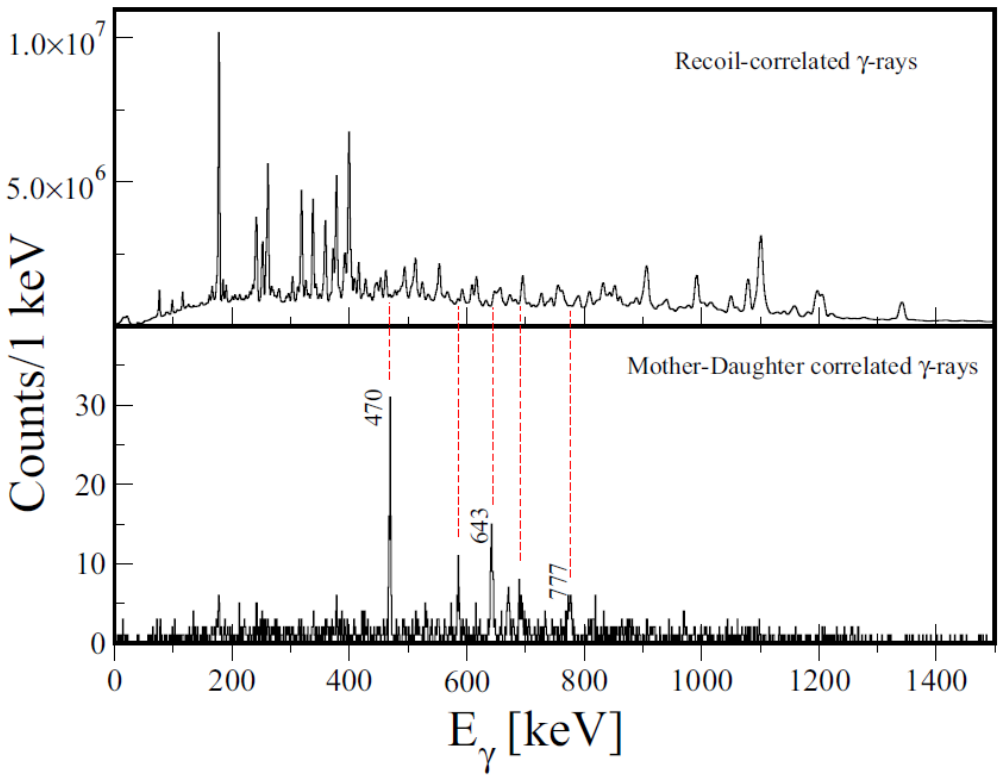

Figure 3.2: Gamma-ray spectra showing prompt γ rays at the target position. The spectrum in the top panel is recoil-gated only, showing all the γ rays detected in the experiment from every fusion-evaporation residue giving a signal in the DSSD. The spectrum in the bottom panel is recoil-decay tagged. The prompt γ rays are correlated by requiring both the subsequent mother ^{110}Xe and daughter ^{106}Te α decays in the same pixel in the DSSD as the recoil implantation. The three strongest transitions assigned to ^{110}Xe are indicated, which cannot be resolved in the total recoil-gated spectrum. The selectivity is greater than 10^{-6}.

$^{40}Ca(^{28}Si,pn)^{66}As$

-Total rate > 1 kHz/ 1pnA

-σ_{pn} ~ few μb << σ_f = n x 100 mb

-additional ”beam stopper” used

- Recoil gating and β-decay tagging

- works for fast β-emitters

Panu Ruotsalainen et. al.,

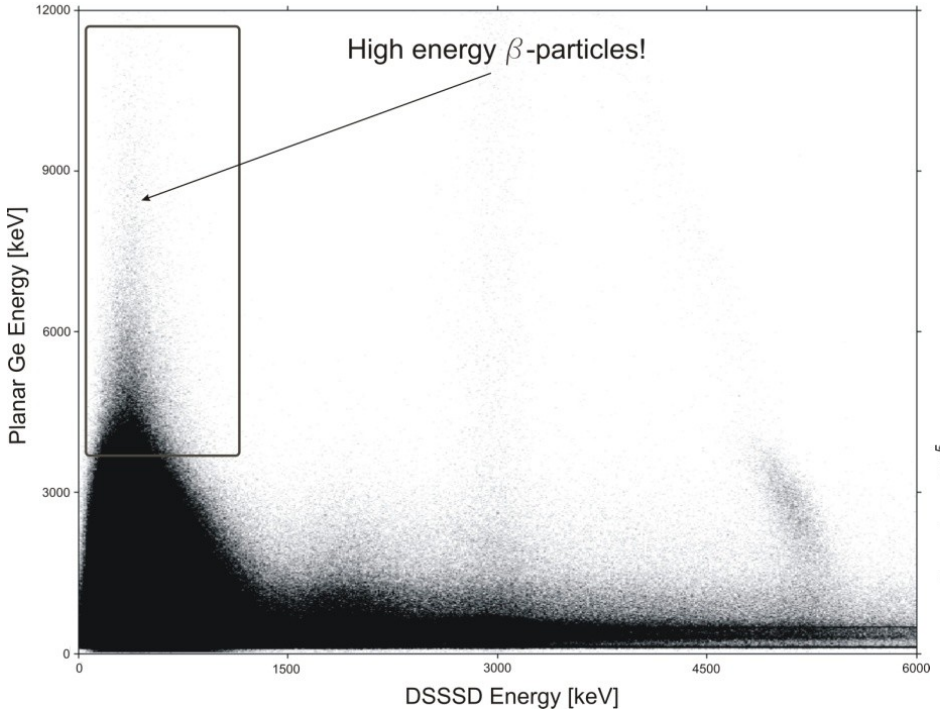

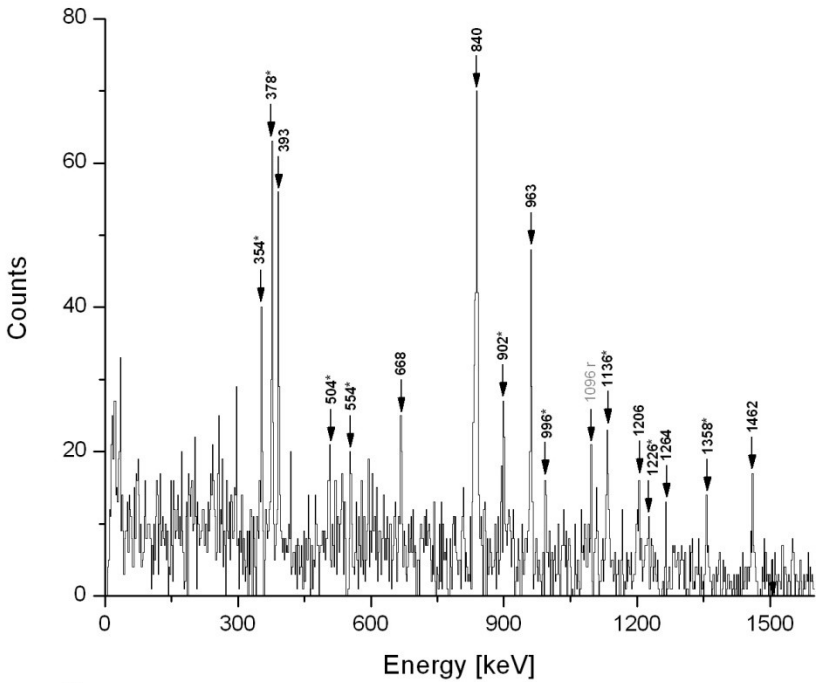

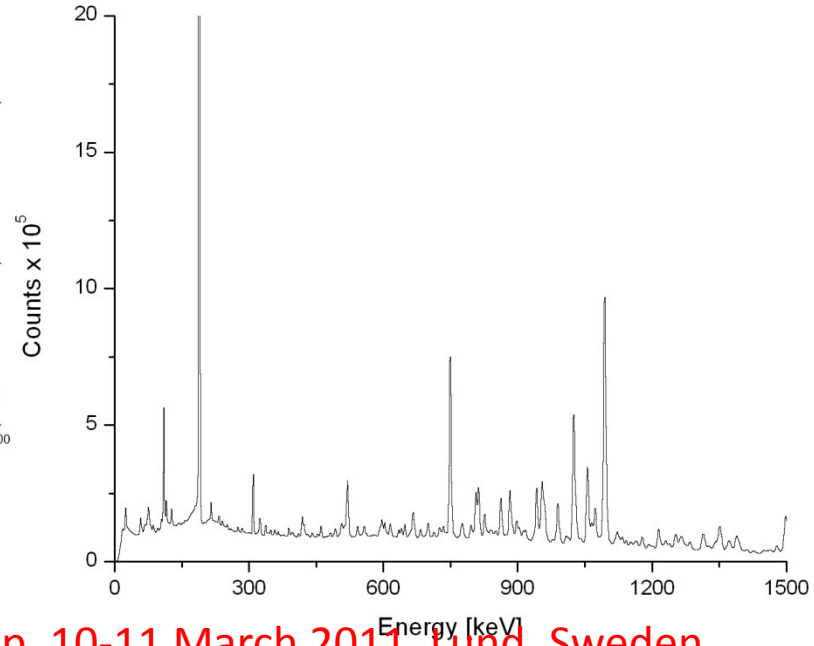

$^{65}Cu + ^{209}Bi$

$@E_{cm}=V_c$ $\Theta_{gr} = 180^o$

RITU tuned for target-like deep-inelastic products

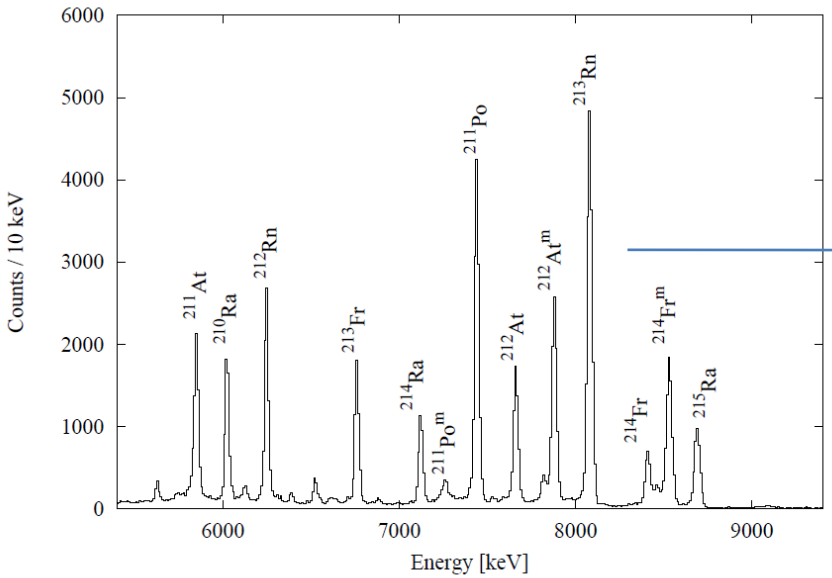

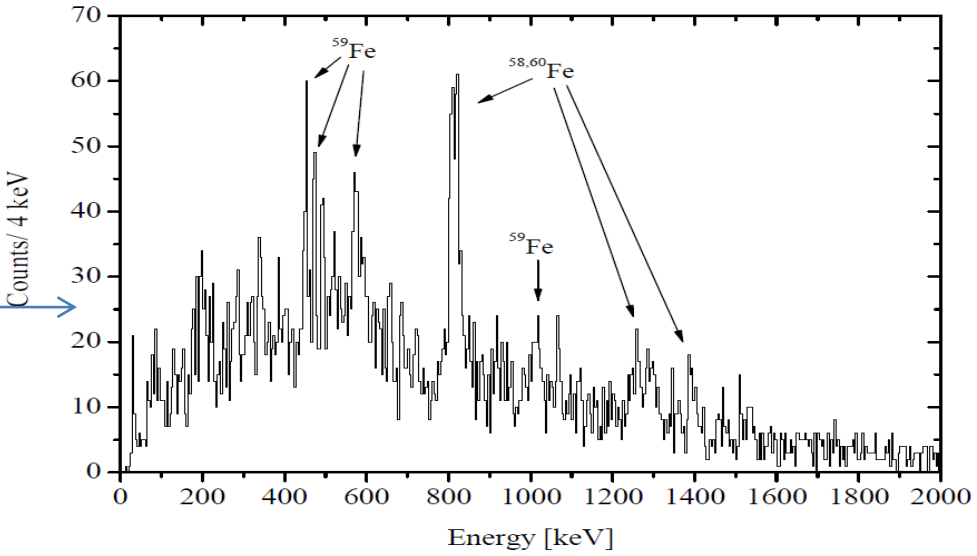

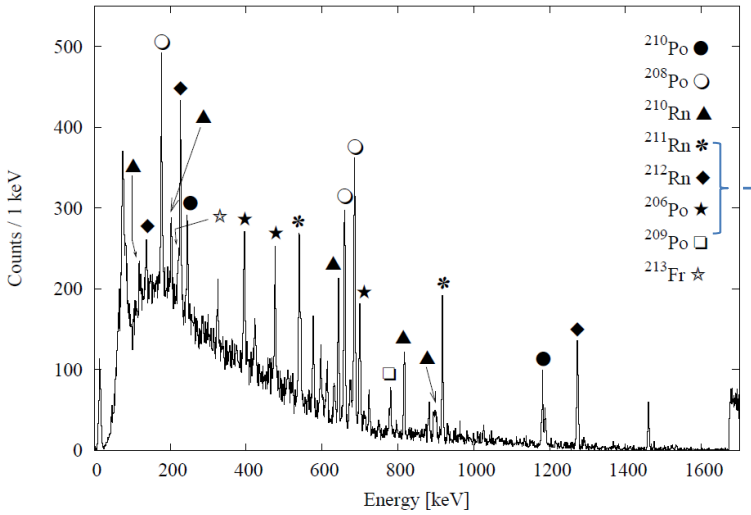

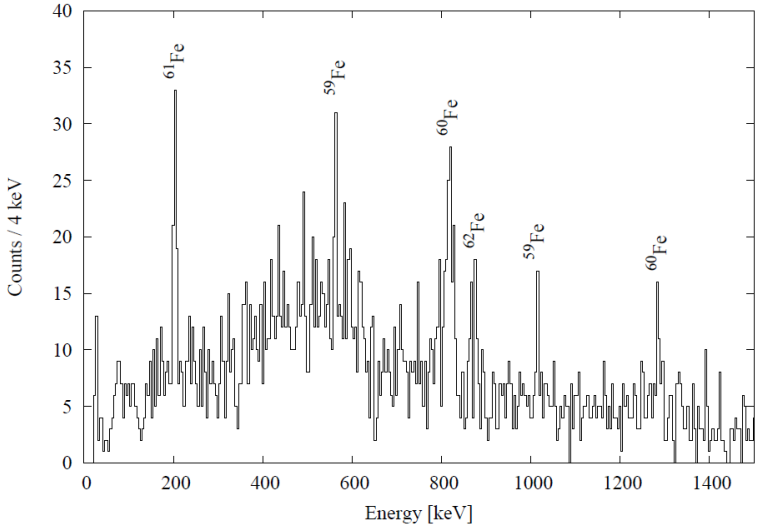

Conclusion

RITU is a very effective and reliable separator above mass 150 where alpha or proton decays (fast isomer decays) can be used for final identification.

RITU can be used also in the lower mass region. However a use of vacuum-mode mass separator will allow to use physical slits to reduce the total counting rates at the focal plane.